Combined PLIF and PIV Laser Imaging Measurements of Heat Release Effects at the Small Scales of Turbulent Reacting Flows

JOHN A. MULLIN, WERNER J.A. DAHM[1] AND JEFFREY M. DONBAR[2]

Laboratory for Turbulence & Combustion (LTC), Department of Aerospace Engineering
The University of Michigan, Ann Arbor, MI 48109-2140 USA

Results are presented from simultaneous planar laser induced fluoresence (PLIF) measurements of CH-radical concentrations and particle image velocimetry (PIV) measurements of velocity fields to assess the relative dynamical importance of dilatation due to heat release in exothermic reacting turbulent shear flows. The measurements are obtained in the far-field of an Re = 18,600 axisymmetric turbulent jet diffusion flame, with a pure oxygen coflow to eliminate fluoresence interference from soot and soot precursors. Various effects contributing to the resolution of the PIV measurements indicate the resulting data to be more than adequately resolved to discern the velocity gradients and associated dilatation. Distributions of the resulting two-dimensional dilatation and vorticity fields were conditioned on the presence of CH to assess their differences inside and outside the reaction zones. Results clearly show an increase in positive dilatation values inside the reaction zones as a consequence of exothermicity. Proper scaling of these heat release effects indicates that significantly larger dilatation values will be present in traditional hydrocarbon-air turbulent jet diffusion flames.

[1] Corresponding author.
[2] Currently Research Scientist, Air Force Research Laboratory, AFRL/PRSS, 1790 Loop Road North, Wright Patterson AFB, OH 45433-7301.

1. Introduction

Developing an understanding of the changes that occur in a turbulent flow as a consequence of the heat released by exothermic reaction, as well as the proper scaling of such heat release effects in terms of fundamental parameters, is an essential bridge between fluid dynamics and combustion science. It is well known that density changes due to heat release can dramatically alter some of the most fundamental properties of turbulent shear flows, even under conditions for which buoyancy effects are negligible. Based on such observations, the relevance to combustion science of results from flows without heat release has long been questioned, with some studies concluding that exothermic reacting flows are manifestly different from nonburning flows.

Heat release leads, in part, to an increase in viscosity and diffusivities with temperature, which can lead to a large reduction in Reynolds number. However provided the resulting Reynolds number is still sufficiently high for the flow to remain fully turbulent, the influence of these changes in transport properties is confined to an increase in the smallest length scales of flow. Heat release can also generate baroclinic vorticity from interactions of density gradients with both hydrostatic and hydrodynamic pressure gradients. The former are "buoyancy effects", which can be quite pronounced even in flows without heat release. However, in flows with negligible buoyancy, Tacina & Dahm (2000) recently showed that the reductions due to heat release in the entrainment and mixing rates of turbulent shear flows can be rigorously accounted for by a general equivalence principle that rescales the density of one of the fluids in the scaling laws for the corresponding nonreacting flow. This further suggests that flows undergoing even highly exothermic reactions can be understood as modifications to their nonreacting counterparts.

Here we examine the effect of the volumetric expansion field produced by changes in the density field due to exothermic reactions occurring within the flow. In particular, we are concerned with the relative importance of the flow produced by volumetric expansion and that produced by the underlying vorticity field in the corresponding nonreacting flow. There is an extensive literature detailing the structure and dynamics of vorticity fields in nonreacting turbulent flows. Developing a comparable understanding of exothermic reacting turbulent flows requires an assessment of how significant the dynamical effects of expansion are due to heat release. It is to such an assessment that the present study is intended to contribute.

We first summarize the theoretical framework used to address this issue, and then present results from planar laser induced fluorescence (PLIF) imaging measurements of CH radical concentrations and simultaneous particle image velocimetry (PIV) measurements of velocity fields in a turbulent jet diffusion flame. From these results we draw conclusions as to the relative effect of volumetric expansion on the underlying turbulent flow field. Although the present data are from a turbulent jet diffusion flame, we are interested in understanding these results and their scaling within the general theoretical framework for heat release effects in turbulent shear flows.

1.1 *Background*

From the Helmholtz decomposition of any vector field, the velocity field $\mathbf{u}(\mathbf{x},t)$ can be separated as

$$\mathrm{u}(\mathrm{x},t) \;=\; \underbrace{\iiint_{x'} ? \,(\mathrm{x}',t)\times \mathrm{K}(\mathrm{x},\mathrm{x}')\,d^3\mathrm{x}'}_{\mathrm{u}_\omega(\mathrm{x},t)} \;+\; \underbrace{\iiint_{x'} q(\mathrm{x}',t)\,\mathrm{K}(\mathrm{x},\mathrm{x}')\,d^3\mathrm{x}'}_{\mathrm{u}_q(\mathrm{x},t)} \;+\; \mathrm{u}_p(\mathrm{x},t) \quad , \tag{1}$$

where the kernel is

$$\mathrm{K}(\mathrm{x},\mathrm{x}') \equiv \frac{1}{4\pi}\frac{\mathrm{x}-\mathrm{x}'}{\left|\mathrm{x}-\mathrm{x}'\right|^3} \quad . \tag{2}$$

In (1), $\mathbf{u}_\omega(\mathbf{x},t)$ is the divergence-free part of the velocity field, where $\mathrm{w}(\mathbf{x},t) \equiv \nabla \times \mathbf{u}(\mathbf{x},t)$ is the vorticity field and the integral relating $\mathrm{w}(\mathbf{x},t)$ and $\mathbf{u}_\omega(\mathbf{x},t)$ is the classical Biot-Savart law. The second term in (1), namely $\mathbf{u}_q(\mathbf{x},t)$, is the curl-free part of the velocity, with $q(\mathbf{x},t) \equiv \nabla\cdot\mathbf{u}(\mathbf{x},t)$ being the dilatation field. Since $\nabla\cdot\mathbf{u} = (\mathrm{DV}/\mathrm{D}t)/\mathrm{V}$, where V is the volume of any fluid element and $\mathrm{D}/\mathrm{D}t$ the Lagrangian time derivative, $q(\mathbf{x},t)$ gives the local, instantaneous rate of volumetric expansion in the flow due to changes in the pressure, temperature, and molecular weight. It is this part that will be of primary interest here. The remaining term $\mathbf{u}_p(\mathbf{x},t)$ in (1) is simply the trivial potential flow that satisfies the boundary conditions for any particular geometry.

From continuity,

$$q(\mathbf{x},t) = -\frac{1}{\rho}\frac{\mathrm{D}\rho}{\mathrm{D}t} \quad , \tag{3}$$

and thus for uniform density flows $q(\mathbf{x},t)$ is zero and $\mathbf{u}_q(\mathbf{x},t)$ in (1) vanishes, and the flow field $\mathbf{u}(\mathbf{x},t)$ in that case results entirely from $\mathbf{u}_\omega(\mathbf{x},t)$ induced by the vorticity field $\mathrm{w}(\mathbf{x},t)$. For exothermic reacting flows, in the zero Mach number limit density changes due to pressure variations are negligible and, as a consequence of the ideal gas law, the dilatation field in (3) is then given by

$$q(\mathbf{x},t) = \frac{1}{T}\frac{\mathrm{D}T}{\mathrm{D}t} - \frac{1}{MW}\frac{\mathrm{D}MW}{\mathrm{D}t} \quad , \tag{4}$$

where $T(\mathbf{x}, t)$ is the temperature field and $MW(\mathbf{x}, t)$ is the molecular weight. For fuel and oxidizer combinations producing relatively high adiabatic flame temperatures, as is usually the case in hydrocarbon combustion, volume changes produced by molecular weight changes in (4) are typically small in comparison with those produced by temperature changes. Moreover, except at conditions locally approaching extinction, the temperature field $T(\mathbf{x}, t)$ in (4) is in near-equilibrium with the local conserved scalar field $\zeta(\mathbf{x}, t)$ via the state relation $T(\zeta)$. Consequently, the dilatation is principally determined as

$$q(\mathbf{x},t) = \frac{dT/d\zeta}{T(\zeta)}\nabla\cdot D\nabla\zeta(\mathbf{x},t) \quad , \tag{5}$$

where D is the scalar diffusivity.

From (5) it is possible to understand certain aspects of the structure and scaling of the dilatation field in turbulent diffusion flames by considering the local diffusion-reaction layer structure formed by the strain-diffusion balance at any point in the flow (*e.g.* Buch & Dahm 1996, 1998). Within such a diffusion and reaction layer (flamelet) between scalar values ζ^+ and ζ^-, the dilatation in (5) necessarily has two zero-points, one at the layer center where $\zeta = {}^1\!/_2\,(\zeta^+ + \zeta^-)$ and thus $\nabla^2\zeta \equiv 0$, and the other at the location of peak temperature T_s, typically very near the stoichiometric value ζ_s, where $dT/d\zeta \equiv 0$. Between these two points the dilatation is negative; elsewhere $q(\mathbf{x}, t)$ is positive and approaches zero outside the diffusion layer. When ${}^1\!/_2\,(\zeta^+ + \zeta^-) \approx \zeta_s$, the negative part vanishes and the dilatation consists of two positive peaks on either side of the layer center.

Within such a diffusion layer, $\nabla\cdot D\nabla\zeta \sim D\,(\zeta^+ + \zeta^-)/\lambda_D{}^2$, $dT/d\zeta \sim (T_s - T_\pm)/\zeta_s$, and $T(\zeta) \sim T_s$, where $\lambda_D \sim (D/\varepsilon)^{1/2}$ is the diffusion layer thickness and $\varepsilon(\mathbf{x}, t)$ is the strain rate (Buch & Dahm 1996, 1998) and where $T_\pm \equiv T(\zeta^\pm)$. Thus from (5) the diltatation scales as

$$q(\mathbf{x},t) \sim \frac{T_s - T_\infty}{T_s}\frac{\zeta^+ - \zeta^-}{\zeta_s}\varepsilon(\mathbf{x},t) \quad . \tag{6}$$

In a turbulent shear flow such as the jet diffusion flame considered here, $\zeta^+ \sim \zeta_c$ and $\zeta^- \sim \zeta_\infty$, where $\zeta_c(x)$ is the local mean centerline scalar value and ζ_∞ is the ambient scalar value. The peak strain rate scales as $\varepsilon \sim (u/\delta)\cdot Re_\delta{}^{1/2}$, where $\delta(x)$ and $u(x)$ are the local outer length and velocity scales that characterize the local mean shear at any axial location x, and $Re_\delta \equiv u\delta/\nu$ is the local outer-scale Reynolds number. These give the dilatation scaling as

$$q \sim \left[\frac{T_s - T_\infty}{T_s}\right]\left[\frac{\zeta_c - \zeta_\infty}{\zeta_s}\right]\left[\frac{u}{\delta}\,Re_\delta^{1/2}\right] \quad . \tag{7}$$

Furthermore, from (1) and (7), and the fact that ω scales the same way as ε in (6), it may be anticipated that

$$\left\|\frac{\mathrm{u}_q(\mathrm{x},t)}{\mathrm{u}_\omega(\mathrm{x},t)}\right\| \sim \left[\frac{T_s - T_\infty}{T_s}\right]\left[\frac{\zeta_c - \zeta_\infty}{\zeta_s}\right] \quad . \tag{8}$$

1.2 *Present study*

The present study is an experimental investigation of $q(\mathbf{x}, t)$ and $\mathrm{w}(\mathbf{x}, t)$ in an exothermic, reacting, turbulent shear flow to assess the relative importance in (1) of $\mathbf{u}_q(\mathbf{x}, t)$ and $\mathbf{u}_\omega(\mathbf{x}, t)$. To this end, we use planar laser induced fluorescence (PLIF) imaging measurements of CH-radical concentrations to mark points within the reaction zones of a turbulent jet diffusion flame. Simultaneous two-color digital particle image velocimetry (PIV) is used to obtained two-dimensional velocity field measurements throughout the the flame. From these data, we obtain the two-dimensional dilatation field $q_{2D}(\mathbf{x}, t)$ throughout the flame. We then conditionally sample the resulting $q_{2D}(\mathbf{x}, t)$ inside and outside the zones marked by CH-radical concentrations, and compare the resulting statistics with proper accounting for the "missing" component of the true dilatation $q(\mathbf{x}, t)$ in the present two-dimensional measurements. This allows a determination of the relative magnitudes of $\mathbf{u}_q(\mathbf{x}, t)$ and $\mathbf{u}_\omega(\mathbf{x}, t)$ in (1) throughout the turbulent flame. From this, we draw conclusions as to the principal effects of heat release in exothermic reacting turbulent shear flows.

2. Experimental apparatus and diagnostics

The present study involves a non-sooting “permanently blue” axisymmetric turbulent jet diffusion flame formed in the burner facility shown in figure 1. The facility consists of a central fuel tube with circular cross-section and 5 mm inner diameter, surrounded by a 150 mm diameter coflow of pure oxygen. The oxygen coflow velocity was 0.3 m/s and the fuel exit velocity was 60 m/s, corresponding to a jet Reynolds number based on the fuel tube diameter and cold gas exit properties of 18,600. The fuel tube runs from the base of the burner through the diffuser and coflow nozzle. From the burner base to a constant-area section containing multiple screens for flow

management, the fuel tube is shrouded by a larger diameter tube. Just after the flow management section, the shroud tapers and the fuel tube maintains a constant diameter. The fuel tube exit is located 15 mm past the exit plane of the coflow nozzle. One-dimensional LDV measurements across the coflow exit plane verified the expected boundary layer profile along the fuel tube wall and showed no sign of separation due to the fuel tube taper. The burner was positioned on a traverse to permit imaging measurements at four downstream locations spanning the entire length of the flame. An exhaust hood located approximately 1.5 m downstream of the fuel tube removed combustion products and PIV seed particles. For measurements at the farthest downstream location, a glass chimney was placed around the coflow to ensure appropriate seed density. Additional details of the apparatus are given in Carter *et al* (1998) and Donbar (1998).

Previous imaging measurements of CH radicals in jet diffusion flames by Stårner *et al* (1992) and Schefer *et al* (1990, 1994) were limited to the region near the flame base to avoid interference from soot precursors and from soot itself. For this reason, the present flame was rendered soot-free over its entire length by using fuel and oxidizer combinations suggested from the laminar flame studies of Du & Axelbaum (1995). For the present study, the fuel mixture was selected to be 30% methane and 70% nitrogen by volume, and the oxidizer to be pure oxygen. The resulting turbulent flame was found to be free from soot interferences, based on fluorescence spectra obtained with a spectrometer and intensified CCD camera.

The pure oxygen coflow also renders the flame three times shorter than when an air coflow is used. The flame is thus in the momentum-dominated regime, in which any buoyancy effects on the flame length or the overall mixing are negligible (*e.g.* Becker & Liang 1978). The oxygen coflow also anchors the flame base to the fuel tube rim, thereby preventing any liftoff of the flame base that would allow premixing of oxygen into the fuel stream.

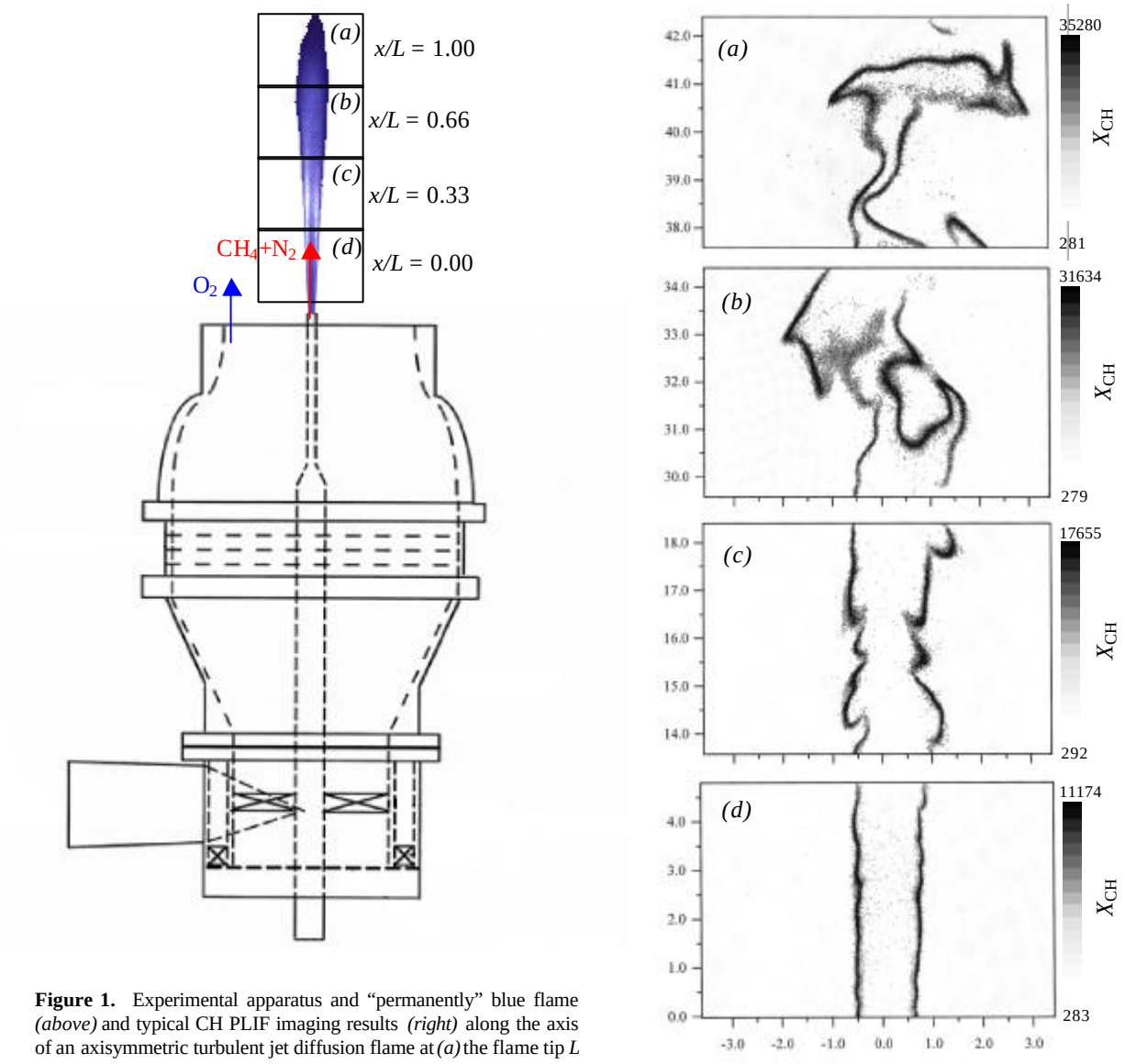

Figure 1. Experimental apparatus and "permanently" blue flame *(above)* and typical CH PLIF imaging results *(right)* along the axis of an axisymmetric turbulent jet diffusion flame at *(a)* the flame tip L = 1.00, *(b)* L = 0.66, *(c)* L = 0.33, *(d)* the flame base L = 0.00.

Moreover, the resulting large value of the stoichiometric fuel mixture fraction ($\zeta_s = 0.56$) shifts the reaction zone toward the jet centerline, where the turbulence intensity is much larger than in a traditional methane-air ($\zeta_s = 0.055$) diffusion flame.

Details are given for the simultaneous CH PLIF and PIV imaging system by Donbar (1998) and for the CH fluorescence scheme by Donbar (1998), Carter *et al* (1998), and Stårner *et al* (1992). Both will be reviewed here only briefly. The 390 nm CH PLIF laser sheet was produced by wavelength-mixing the 616.4 nm output of a dye laser with the residual 1064 nm beam from the Nd:YAG pump laser. The resulting 390 and 616 nm beams were then separated. The red 616 nm beam was used together with a green 532 nm beam from a second Nd:YAG laser to provide two color-separated PIV sheets. The 390 nm CH PLIF beam was then formed into a nominally 35 mm high laser sheet having an average FWHM thickness of approximately 200 μm. The 532 and 616 nm PIV beams were formed into nominally 35 mm high laser sheets with approximately 600-800 μm FWHM thickness. The thickness of the PIV sheets is somewhat smaller than the size of the 128-pixel square interrogation box used in the PIV processing. The delay between the beams was set with a digital delay generator and the beam energies were 15-20 mJ at the test section.

CH fluorescence was obtained by tuning the frequency-mixed output of a Nd:YAG-pumped dye laser to the $Q_1(7.5)$ transition of the $B^2\Sigma^- - X^2\Pi$ ($\nu' = 0$, $\nu'' = 0$) band ($\lambda = 390.30$ nm). Fluorescence was then collected from the A-X (1,1), (0,0) and B-X (0,1) bands ($\lambda = 420 - 440$ nm) Luque *et al*. (1996). This approach provided sufficient separation between pump and detection wavelengths to reject the incident light. A Schott KV-418 color glass filter provided greater than 6 orders of magnitude of rejection at 390 nm while maintaining 90% transmission at 430 nm. Furthermore, the LIF signal with this excitation/detection scheme is significantly greater than that provided by A-X (0,0) excitation and A-X (0,1) detection. A 36×24 mm field-of-view was focused onto a 13.2×8.8 mm Princeton Instruments (PI) intensified CCD array composed of 576×384 pixels. To improve the signal-to-noise ratio, each 2×2 pixel region was spatially averaged.

The PIV measurements used an appropriate number density of 0.5 μm Al_2O_3 seed particles to produce a high percentage (> 95%) of good vectors. The particle images were recorded using a color Kodak DCS460 CCD camera (2036 × 3060 pixels, each 9-μm square). The digital two-color PIV system permitted resolution of directional ambiguity and the use of cross-correlation techniques to obtain particle displacements. The particle images were converted to velocity fields using custom software described Gogineni *et al* (1998). Bad vectors were replaced by interpolated values from surrounding points, and the resulting velocity fields were subsequently filtered with a spectrally-sharp filter.

CH PLIF imaging measurements and simultaneous PIV measurements were made at four downstream locations as shown in figure 1 (Donbar 1998). Only data from the $x/L = 0.66$ location in figure 1*b* is used in the present study, since at that location the turbulent diffusion flame marked by the instantaneous CH field is highly wrinkled.

3. Resolution

The resolution limits introduced by the measurements and data processing are of key importance, since this study uses velocity measurements to make assessments of velocity gradient quantities. There are two main issues involved. The first is the implicit filtering of the velocity gradients $\nabla\mathbf{u}(\mathbf{x}, t)$ that results from the finite resolution of the velocity field measurements. The second is the resolution of the CH PLIF measurements, since these data are used to identify points within the exothermic reaction zone.

Regarding the latter, CH-layer thicknesses were obtained from the PLIF data via one-dimensional horizontal intersections and two-dimensional layer-normal intersections through the CH layers. These yielded average FWHM thicknesses of $\lambda_{CH,\,FWHM} \approx 730$ μm and 430 μm, respectively, at the present $x/L = 0.66$ measurement location (Donbar 1998, Donbar *et al* 2000). These values are significantly larger than the laser sheet thickness, but still exceed the true layer thicknesses due to geometric factors relating the orientation of the true layer-normal vector to the intersection direction. Since the assumption of isotropy in the CH-layer orientations appears justified at this x/L location (*e.g.* see figure 1*b*), the method of Buch & Dahm (1998) can be used to obtain the true CH-layer thickness from these one- and two-dimensional estimates. This indicates an average true thickness of $\lambda_{CH,\,FWHM} \approx 350$ μm. That value agrees with $\lambda_{CH,\,FWHM} \approx 200 - 450$ μm from OPPDIFF simulations for detailed chemical kinetics in a strained diffusion flame between the pure oxygen coflow and a mixture of fuel and combustion products ($\zeta = 0.8$) at strain rates from $100\ s^{-1} \le \varepsilon \le 1000\ s^{-1}$. Moreover, such simulations give the ratio of dilatation-layer thickness to CH-layer thicknesses as $6 < (\lambda_q/\lambda_{CH}) < 9$ for strain rates ranging from $100\ s^{-1} \le \varepsilon \le 10{,}000\ s^{-1}$. From this, the average dilatation-layer thickness at the measurement location is $\lambda_{q,FWHM} \approx 2100$ μm. It is this length scale that must be compared with the resolution length scale of the PIV measurements to determine the extent to which these data resolve the dilatation field $\nabla\cdot\mathbf{u}(\mathbf{x}, t)$.

There are five principal factors that contribute to the resolution of the PIV measurements, namely *i)* the PIV laser sheet thickness Δ_1, *ii)* the PIV correlation window size Δ_2, *iii)* the typical bad-vector replacement region size Δ_3, *iv)* the PIV processing filter scale Δ_4, and *v)* the spectrally-sharp derivative filter scale Δ_5.

As noted in §2, the FWHM thickness of both the red and green PIV laser sheets at the jet centerline was found from direct measurements to be $\Delta_1 \approx$ 600-800 μm. The 128×128 pixel PIV correlation window, together with the pixel size and image ratio, effectively filtered the velocity field at a scale of approximately $\Delta_2 \approx 1495$ μm. Explicit filtering performed as part of the PIV processing was done at a scale of $\Delta_3 \approx 400$ μm. From the spacing between vectors produced by the PIV processing, the size of the largest bad-vector regions was around $\Delta_4 \approx 400$ μm. Lastly, the velocity gradient fields $\nabla\mathbf{u}(\mathbf{x},t)$ produced by the resulting vectors were processed with a spectrally sharp filter at a scale of $\Delta_5 \approx 800$ μm.

Since these contributions to the net PIV resolution are essentially independent, the resulting velocity gradient fields are resolved to a length scale of approximately $\Delta_{net} \approx 1920$ μm. This effective PIV resolution scale must be compared with the $\lambda_{q,\,FWHM} \approx 2100$ μm scale of the dilatation field obtained above. The dilatation field that results from filtering at this scale is related to the true dilatation field $q(\mathbf{x},t)$ as

$$\tilde{q}(\mathrm{x},t) = \left[1+(\Delta_{net}/\lambda_q)^2\right]^{-1/2} q(\mathrm{x},t) \quad . \tag{9}$$

From (9) and the values given above, the measured dilatation is approximately 0.74 times the true dilatation, indicating that the resolution capabilities of both the CH imaging measurements and the PIV measurements are adequate to assess the effects of the dilatation field produced by combustion heat release in this experiment.

4. Results and discussion

Figure 2 shows typical profiles of the dilatation q from (4) and the CH mole fraction X_{CH} from OPPDIFF simulations of a strained diffusion and reaction layer, in this case between a $\zeta^+ = 0.8$ mixture of the present fuel and combustion products and the $\zeta^- = 0$ pure oxygen coflow, at a strain rate of $\varepsilon = 100\ s^{-1}$. As expected from §1.1, since $^1/_2\,(\zeta^+ + \zeta^-) \approx \zeta_s$ the dilatation field essentially consists of two positive peaks on either side of the layer center. CH radical concentrations are roughly centered within the dilatation zone on the fuel-rich side of the reaction layer. This basic structure is maintained for strain rates ε in excess of 30,000 s^{-1}, showing principally the expected $\varepsilon^{-1/2}$ reduction in the length scale λ_D of the diffusion and reaction layer together with a weak ($O\,\varepsilon^{1/8}$) nonequilibrium broadening of the CH zone relative to λ_D and variation in peak CH concentration with ε. Consequently, within regions marked by measurable CH concentrations in the present imaging data, the dilatation $q(\mathbf{x},t)$ due to heat release is significant.

Examples of four typical instantaneous CH fields, from the PLIF imaging measurements at $x/L = 0.66$, are shown in figure 3 (see also Donbar 1998). High concentrations of CH radicals are located in relatively thin, wrinkled, sheet-like reaction layers that are contorted by the underlying turbulent flow, consistent with various "strained laminar flamelet" models of turbulent diffusion flames. As noted from figure 2, these thin layers of high CH concentration contain large dilatation values due to reaction heat release. In the remainder of the diffusion and reaction layers, roughly centered around these CH layers and with a thickness approximately 6-9 times greater than the CH layers, there can be appreciable dilatation due to heat release. However outside the diffusion and reaction layers, the dilatation is zero. Since diffusion layers containing the stoichiometric mixture fraction (*i.e.*, diffusion and reaction layers) occupy only a small fraction of the total flow volume (*e.g.* see figures 2 - 5 of Buch & Dahm 1998), the dilatation will be zero throughout most of the regions where no CH is found.

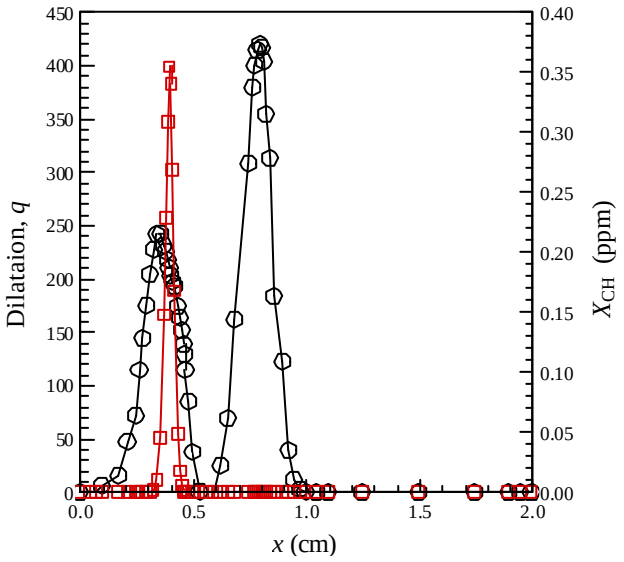

Figure 2. Dilatation q (○) and CH radical concentration X_{CH} (□) across a one-dimensional strained diffusion flame at $\varepsilon = 100\ s^{-1}$, from OPPDIFF calculations.

Figure 4 shows two-dimensional velocity vectors obtained from the present PIV measurements. The velocity field in each panel was obtained at the same instant of time as the CH field in the corresponding panel in figure 3. Large velocity gradients are apparent in these fields. Moreover, by comparing the corresponding panels in figures 3

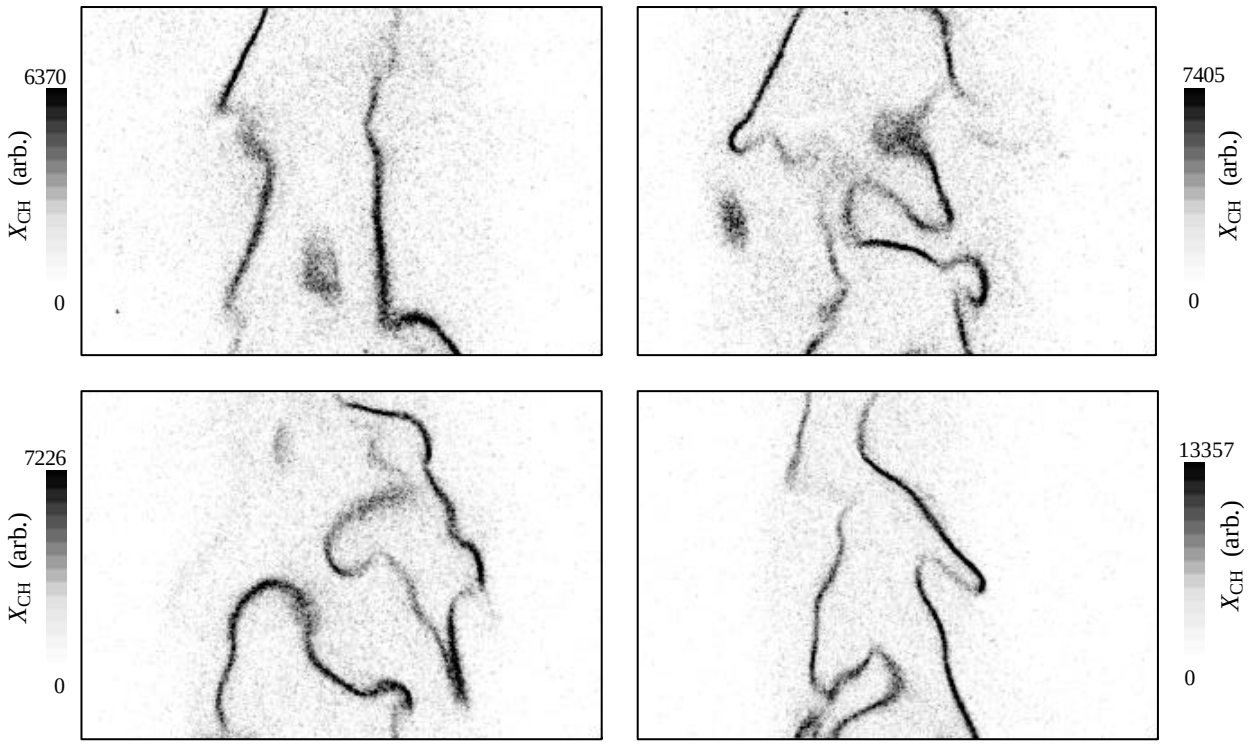

Figure 3. Typical CH concentrations fields $X_{CH}(\mathbf{x},t)$ from CH PLIF imaging in the far-field of the axisymmetric turbulent jet flame ($x/L = 0.66$), showing the thin, highly wrinkled, sheet-like structure of the CH layers.

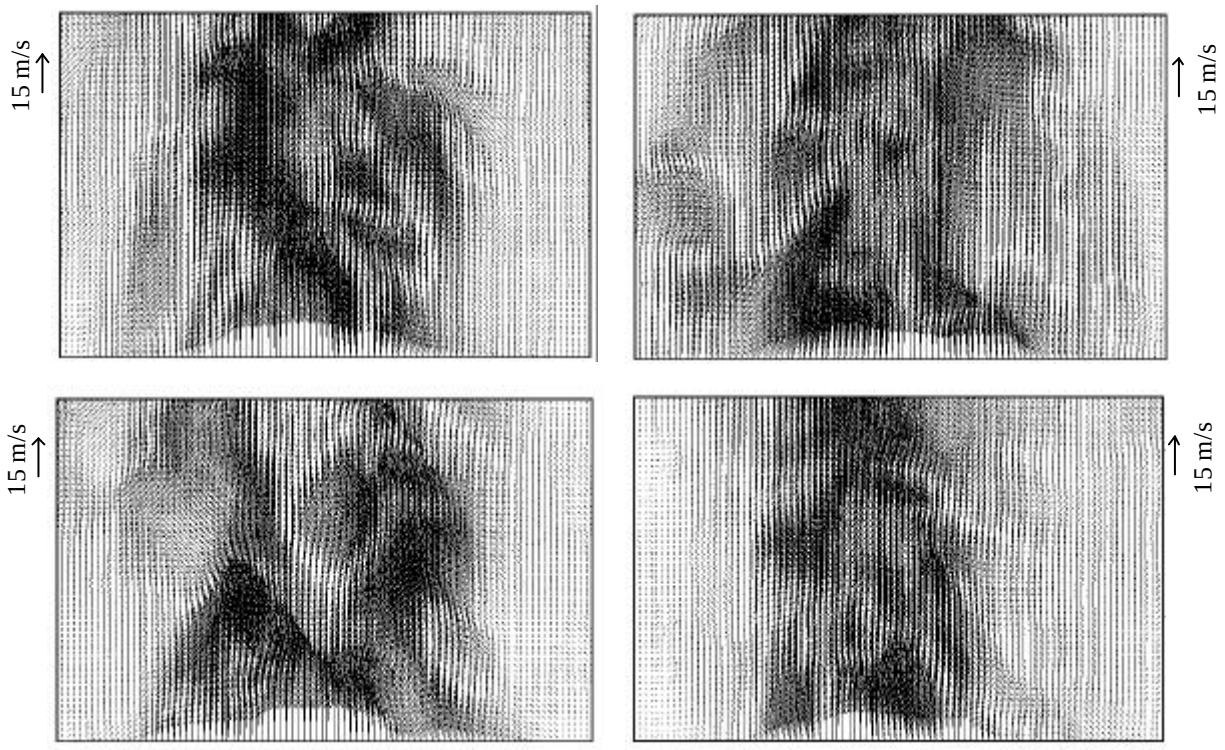

Figure 4. Typical velocity vector fields $\mathbf{u}(\mathbf{x},t)$ from two-dimensional PIV measurements corresponding to each of the CH concentration fields in figure 3.

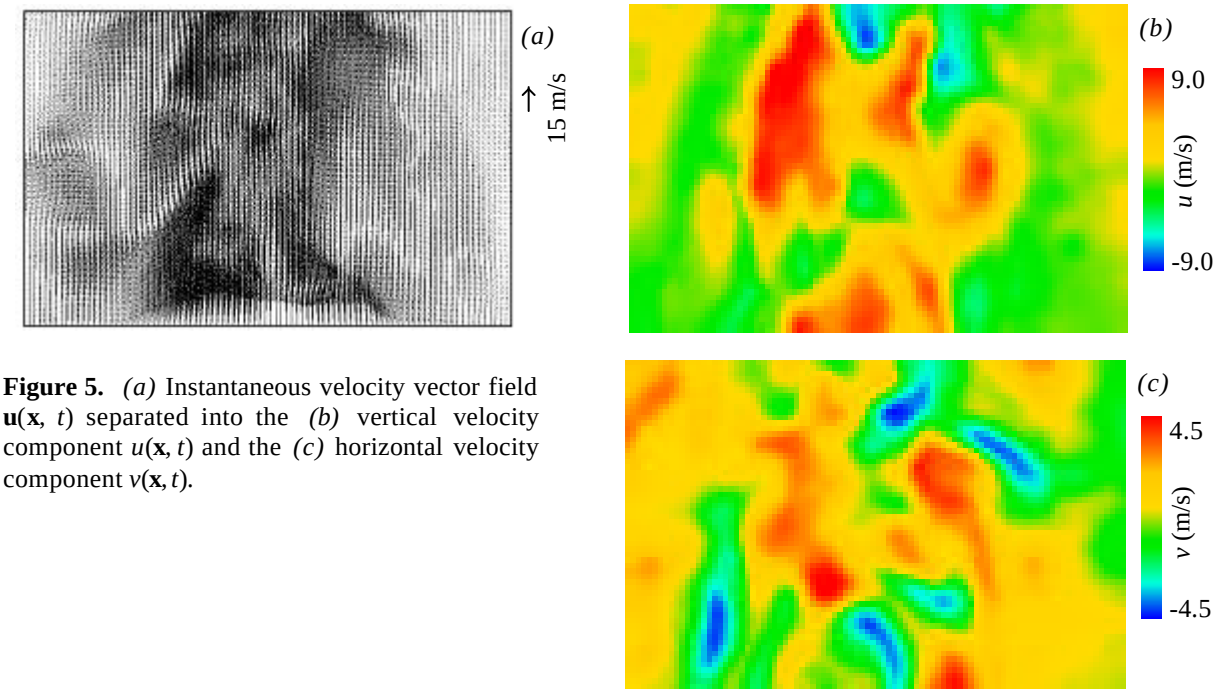

Figure 5. *(a)* Instantaneous velocity vector field $\mathbf{u}(\mathbf{x}, t)$ separated into the *(b)* vertical velocity component $u(\mathbf{x}, t)$ and the *(c)* horizontal velocity component $v(\mathbf{x}, t)$.

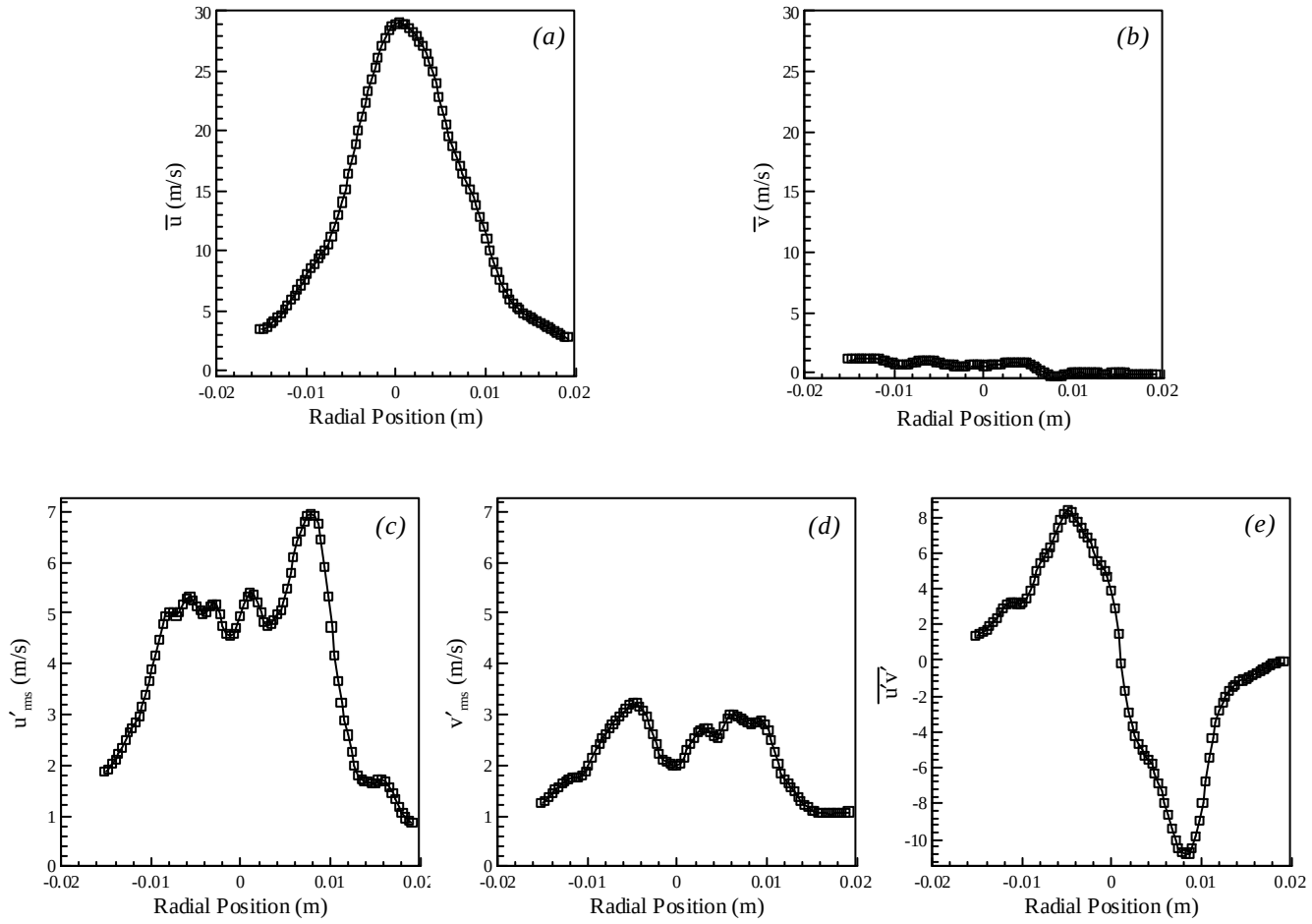

Figure 6. Radial profiles of various velocity statistics, showing *(a)* mean streamwise velocity $\overline{u}$, *(b)* mean radial velocity $\overline{v}$, *(c)* streamwise rms velocity u'_{rms}, *(d)* radial rms velocity v'_{rms}, and *(e)* Reynolds stress component $\overline{u'v'}$.

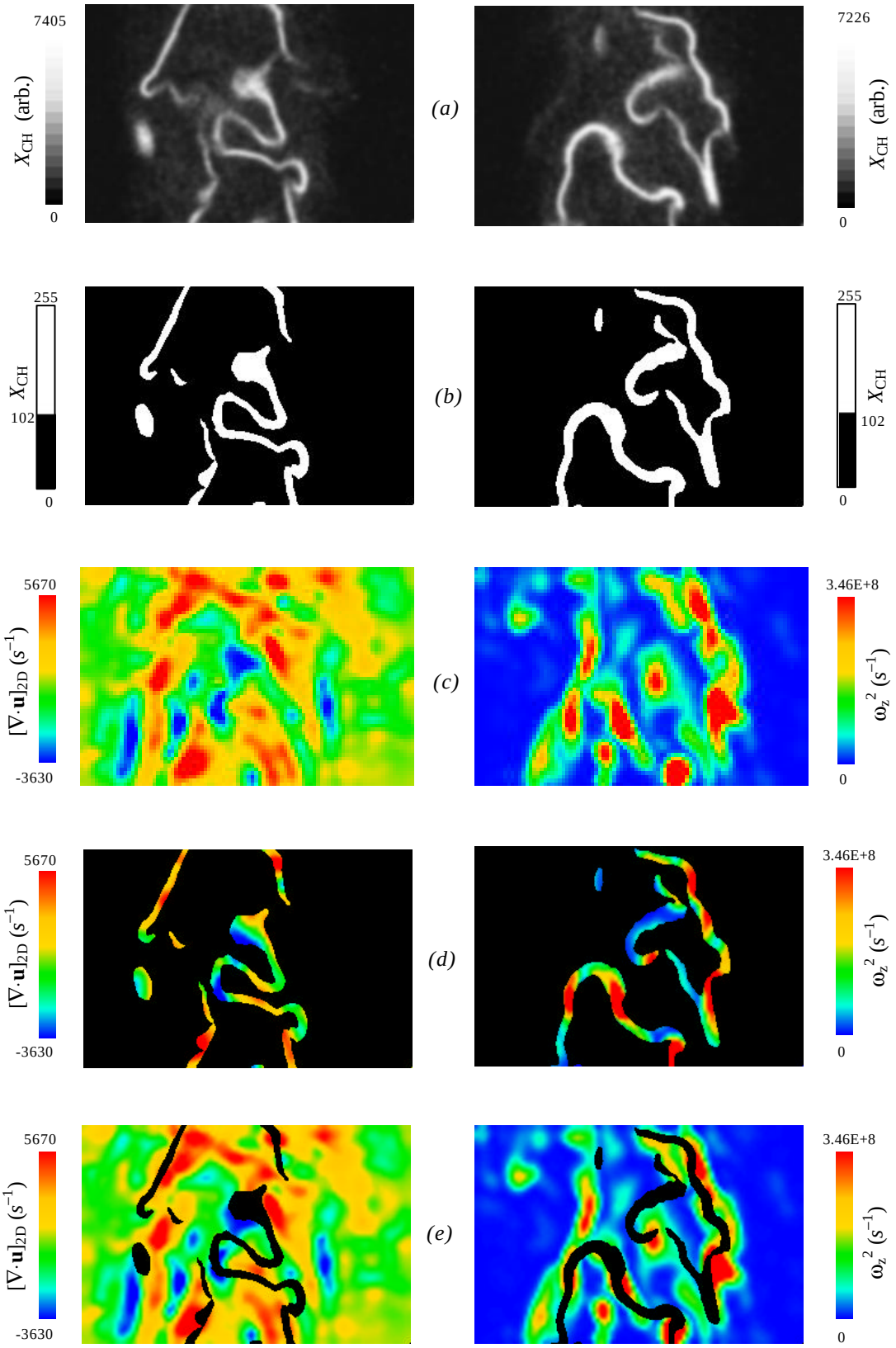

Figure 7. Effect of the reaction zone on the dilatation field and the in-plane enstrophy field, showing (*a*) CH concentration field $X_{CH}(\mathbf{x},t)$, (*b*) the CH zone defined by an X_{CH} threshold value, (*c*) the corresponding dilatation field $[\nabla \cdot u]_{2D}$ and in-plane enstrophy field ω_z^2, (*d*) the dilatation field $[\nabla \cdot u]_{2D}$ and the in-plane enstrophy field ω_z^2 within the CH zone defined by the threshold value, (*e*) the dilatation field $[\nabla \cdot u]_{2D}$ and in-plane enstrophy field ω_z^2 outside the CH zone.

and 4, it is apparent that large gradients in velocity often occur across the thin CH layers. Each of the velocity vector planes is separated into its *u*- and *v*-components, corresponding to the vertical and lateral directions in figure 5*a*, to produce planes of $u(\mathbf{x},t)$ and $v(\mathbf{x},t)$ as shown in figures 5*b*,*c*.

Figure 4 shows two-dimensional velocity vectors obtained from the present PIV measurements. The velocity field in each panel was obtained at the same instant of time as the CH field in the corresponding panel in figure 3. Large velocity gradients are apparent in these fields. Moreover, by comparing the corresponding panels in figures 3 and 4, it is apparent that large gradients in velocity often occur across the thin CH layers. Each of the velocity vector planes is separated into its u- and v-components, corresponding to the vertical and lateral directions in figure 5*a*, to produce planes of $u(\mathbf{x},t)$ and $v(\mathbf{x},t)$ as shown in figures 5*b*,*c*.

For validation purposes, each of these instantaneous velocity component planes was ensemble-averaged and then integrated along the vertical (*i.e.*, *x*) direction to produce the mean velocity component profiles shown in figures 6*a*,*b*. Despite the fact that only 10 such planes were used for each of the velocity components, the resulting mean profiles appear to be reasonably converged. In particular, the *u*-component profile in figure 6*a* agrees well with classical measurements, and $v \ll u$ in figure 6*b* as required by continuity and the growth rate of the turbulent jet. Figures 6*c*-*e* show the Reynolds stress components accessible by these two-dimensional PIV measurements. While the *u*- and *v*-fluctuation correlations in figures 6*c*,*d* show incomplete convergence, the cross correlation in figure 6*e* is relatively well converged and agrees with classical measurements.

Two-dimensional velocity field measurements such as those in figures 4 and 5 do not permit full access to the true dilatation field $\nabla\cdot\mathbf{u}(\mathbf{x},t)$, but instead allow only the "two-dimensional dilatation field" $(\nabla\cdot\mathbf{u})_{2D}$, defined as

$$(\nabla\cdot\mathbf{u})_{2D} \equiv \left(\frac{\partial u}{\partial x}\right)+\left(\frac{\partial v}{\partial y}\right), \tag{10}$$

to be obtained. Since $\mathbf{u}(\mathbf{x},t) = \mathbf{u}_\omega(\mathbf{x},t) + \mathbf{u}_q(\mathbf{x},t)$ from (1), and with $\nabla\cdot\mathbf{u}_\omega \equiv 0$ and $\nabla\cdot\mathbf{u}_q \equiv q(\mathbf{x},t)$,

$$(\nabla\cdot\mathbf{u})_{2D} \equiv -\left(\frac{\partial w_\omega}{\partial z}\right)-\left(\frac{\partial w_q}{\partial z}\right)+q(\mathbf{x},t)\,. \tag{11}$$

Outside the diffusion and reaction layers $q \equiv 0$, while inside these layers $q \neq 0$. Comparing values of $(\nabla\cdot\mathbf{u})_{2D}$ inside and outside the diffusion and reaction layers thus allows assessment of the relative magnitude of the dilatation field $q(\mathbf{x},t)$.

However as figure 2 shows, with the present CH imaging measurements it is not possible to unambiguously separate points within the diffusion and reaction layers from those outside them. Nevertheless, regions of significant CH concentration are clearly within the diffusion and reaction layers, and thus clearly correspond to points where $q \neq 0$. Regions with essentially zero CH concentration include points within the diffusion and reaction layer at values of $\zeta(\mathbf{x},t)$ sufficiently close to ζ_s that $q \neq 0$, as well as a *much* larger number of points at values of $\zeta(\mathbf{x},t)$ sufficiently far from ζ_s that $q \equiv 0$. By collecting statistics over points having essentially zero CH concentration, the contribution from $q(\mathbf{x},t)$ in (11) to $(\nabla\cdot\mathbf{u})_{2D}$ will thus be small. In this manner, by comparing conditional statistics of $(\nabla\cdot\mathbf{u})_{2D}$ inside and outside the high-CH layers, it is possible to assess the relative magnitude of $q(\mathbf{x},t)$ due to heat release.

In figure 7, the left-hand column thus shows the decomposition of the two-dimensional dilatation field $(\nabla\cdot\mathbf{u})_{2D}$ into regions inside and outside the regions marked by the CH concentration field. The right-hand column is a similar decomposition for the vorticity vector component $w_z^2(\mathbf{x},t)$ in a different image. In each case, a threshold value of the CH number density in figure 7*a* was chosen that effectively marks the region within which the CH radicals are concentrated. Results obtained for different threshold values were virtually independent of the precise threshold value used. Each image was thus separated into regions inside and outside the CH layers, as shown in figure 7*b*. Each of the $(\nabla\cdot\mathbf{u})_{2D}$ and $w_z^2(\mathbf{x},t)$ fields as shown in figure 7*c* was then separated as shown in figures 7*d*,*e*. This was done for each individual simultaneous CH-PLIF and PIV image pair in the data set.

Values of $(\nabla\cdot\mathbf{u})_{2D}$ and $w_z^2(\mathbf{x},t)$ were thus obtained inside and outside the CH layers and used to generate the conditional probability densities shown in figures 8 and 9. It is apparent in figures 8*c* and 9*c* that, inside the CH layers, there is an increase in positive values of $(\nabla\cdot\mathbf{u})_{2D}$ and a shift to larger values of $w_z^2(\mathbf{x},t)$. Moreover, since isotropy in the velocity gradients and in the CH-layer orientations appears justified (*e.g.* see figure 1*c*)

$$\left\langle\frac{\partial w_\omega}{\partial z}\right\rangle \equiv 0 \qquad \text{and} \qquad \left\langle\frac{\partial w_q}{\partial z}\right\rangle \equiv \frac{1}{3}\left\langle q(\mathbf{x},t)\right\rangle \quad . \tag{12}$$

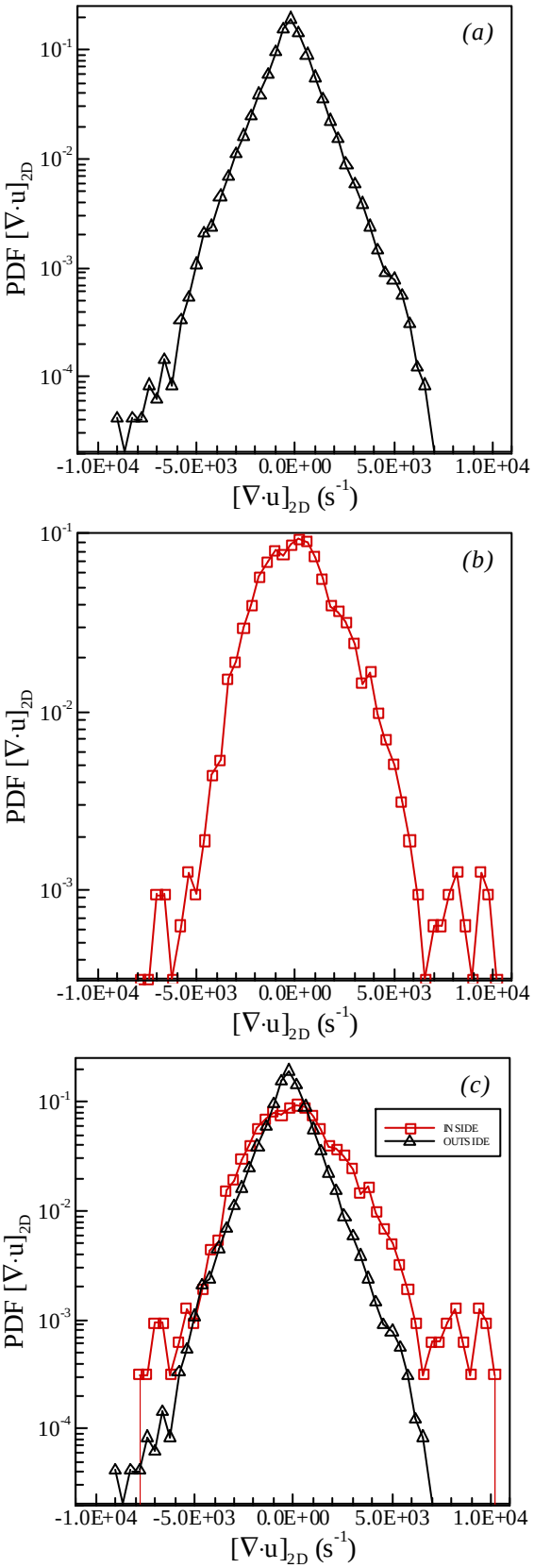

Figure 8. Probability densities of $[\nabla \cdot u]_{2D}$ obtained *(a)* outside the CH zone, *(b)* inside the CH zone, and *(c)* both inside and outside the CH zone.

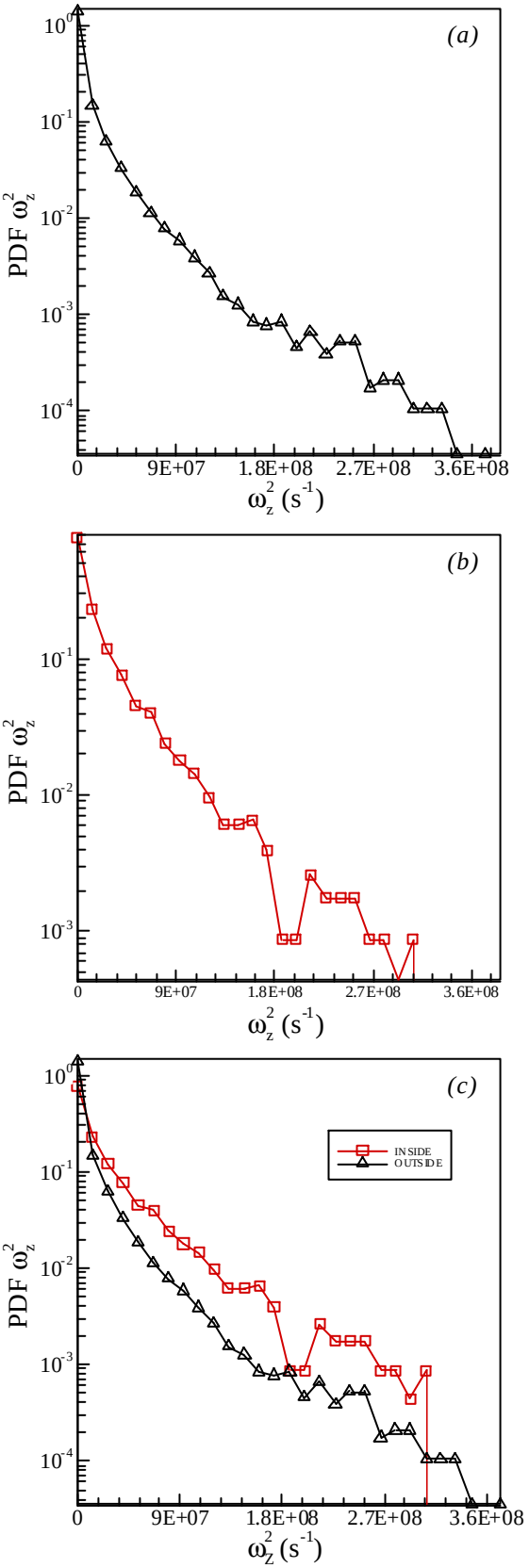

Figure 9. Probability densities of ω_z^2 obtained *(a)* outside the CH zone, *(b)* inside the CH zone, and *(c)* both inside and outside the CH zone.

Thus $\langle \nabla \cdot \mathbf{u}_{2D} \rangle$ outside the CH layers should be essentially zero, and $\langle \nabla \cdot \mathbf{u}_{2D} \rangle$ within the CH layers should be $2/3\langle q \rangle$. This is consistent with figure 8, where figure 8*a* confirms that $(\nabla \cdot \mathbf{u})_{2D}$ outside the CH layers is essentially symmetric and hence has a mean value very near zero, while figure 8*b* confirms that $(\nabla \cdot \mathbf{u})_{2D}$ within the CH layers is clearly skewed to positive values that correspond to volumetric expansion due to exothermic reaction, as suggested by figure 2. The distribution in figure 8*b* gives a mean value $\langle \nabla \cdot \mathbf{u}_{2D} \rangle \approx 137\ s^{-1}$, corresponding to $\langle q \rangle \approx 205\ s^{-1}$, within the CH layers. From the resolution estimates in §3 this would suggest a true mean dilatation value within the CH layers of $\langle q \rangle \approx 275\ s^{-1}$. This could be scaled as indicated in (7) to give a presumably quasi-universal value for the mean dilatation values within the diffusion and reaction layers in exothermic turbulent reacting shear flows.

5. Conclusions

The present results have shown how simultaneous two-dimensional CH PLIF and PIV measurements can be used to assess the effect of dilatation due to heat release in a turbulent shear flow. Conditional statistics of $(\nabla \cdot \mathbf{u})_{2D}$ based on the CH concentration relative to threshold value allow the effect of exothermicity to be discerned. For the present conditions, relatively large positive values of $(\nabla \cdot \mathbf{u})_{2D}$ are found within the CH layers. These yield the average dilatation due to heat release as $275\ s^{-1}$.

Acknowledgements

This work was supported, in part, by the Air Force Office of Scientific Research (AFOSR) under AFOSR Contract Nos. F49620-95-1-0115 and F49620-98-1-0003, with Dr. Julian M. Tishkoff as Technical Monitor. The technical assistance of Dr. Cam Carter at AFRL/PRSS Wright-Patterson AFB, and discussions with Prof. Jim Driscoll at Michigan, are gratefully acknowledged.

References

Becker, H.A. and Liang, D. (1978) Visible length of vertical free turbulent diffusion flames. *Combust. Flame* **32**, 115-137.

Buch, K.A. and Dahm, W.J.A. (1996) Experimental study of the fine-scale structure of conserved scalar mixing in turbulent shear flows. Part 1. *Sc* >> 1. *J. Fluid Mech*. **317**, 21-71.

Buch, K.A. and Dahm, W.J.A. (1998) Experimental study of the fine-scale structure of conserved scalar mixing in turbulent shear flows. Part 1. *Sc* ≈ 1. *J. Fluid Mech*. **364**, 1-29.

Carter, C.D., Donbar, J. M. and Driscoll, J.F. (1998) Simultaneous CH-PIV imaging of turbulent nonpremixed flames. *Appl, Phys. B* **66**, 129-132.

Donbar, J.M. (1998) Reaction zone structure and velocity measurements in permanently blue nonpremixed jet flames. *Ph.D. Thesis*, The University of Michigan, Ann Arbor.

Donbar, J.M., Driscoll, J.F. and Carter, C.D. (2000) Reaction zone structure in turbulent nonpremixed jet flames from CH-OH PLIF images. To appear in *Combust. Flame* .

Du, J. and Axelbaum, R.L. (1995) The effect of flame structure on soot-particle inception in diffusion flames. *Combust. Flame* **100**, 367-375.

Gogineni, S., Goss, L., Pestian, D. and Rivir, R. (1998) Two-color digital PIV employing a single CCD camera. *Exp. Fluids* **25**, 320-328.

Luque, J. and Crosley, D.R. (1996) *LIFBASE Version 1.1*, SRI Report MP96-001, SRI, Palo Alto.

Schefer, R.W., Namazian, M. and Kelly, J. (1990) CH, OH, and CH_4 concentration measurements in a lifted turbulent-jet flame. *Proc. Twenty-Third Symp. (Int'l.) Comb*. pp. 669-676, The Combustion Institute, Pittsburgh.

Schefer, R.W., Namazian, M., Filtopoulos, E.E.J. and Kelly, J. (1994) Temporal evolution of turbulence/chemistry interactions in lifted, turbulent-jet flames. *Proc. Twenty-Fifth Symp. (Int'l.) Comb*. pp. 1223-1231, The Combustion Institute, Pittsburgh.

Stårner, S.H., Bilger, R. W., Dibble, R.W., Barlow, R.S., Fourguette, D.C. and Long, M.B. (1992) Joint planar CH and OH LIF imaging in piloted turbulent jet diffusion flames near extinction. *Proc. Twenty-Fourth Symp. (Int'l.) Comb*. pp. 341-349, The Combustion Institute, Pittsburgh.

Tacina, K.M. and Dahm, W.J.A. (2000) Effects of heat release on turbulent shear flows. Part I. A general equivalence principle for nonbuoyant flows and its application to turbulent jet flames. To appear in *J. Fluid Mech.*

Watson, K.A., Lyons, K.M., Donbar, J.M. and Carter, C.D. (1999) Scalar and velocity field measurements in a lifted CH_4-air diffusion flame. *Combust. Flame* **117**, 257-271.